

A DNAzyme-powered cross-catalytic circuit for amplified intracellular imaging

*Lana Zou, † Qiong Wu, † Yangjie Zhou, Xue Gong, Xiaoqing Liu, and Fuan Wang**

Key Laboratory of Analytical Chemistry for Biology and Medicine (Ministry of Education), College of Chemistry and Molecular Sciences, Wuhan University, Wuhan, P. R. China

* To whom correspondence should be addressed. E-mail: fuanwang@whu.edu.cn.

† These authors contributed equally to the paper as first authors.

Supporting Information

Table of Contents

Experimental Section	S2
Modeling Section	S3
Table S1. Rate constants of the cross-catalytic circuit.....	S5
Table S2. Rate constants of the non-feedback circuit.....	S6
Table S3. Sequences of all oligonucleotides used in this work.....	S7
Table S4. Comparison of different enzyme-free strategies for microRNA detection.....	S8
Figure S1. Schematic illustration of the CHA reaction.....	S9
Figure S2. Demonstration of the lead-in CHA-DNAzyme concatenation.....	S10
Figure S3. Demonstration of the reverse DNAzyme-CHA concatenation.....	S11
Figure S4. Optimization of reaction buffer.....	S12
Figure S5. Optimization of reaction temperature.....	S13
Figure S6. Optimization of substrate blocker L	S14
Figure S7. Optimization of the substrate to blocker (S/L) ratio.....	S15
Figure S8. Sensitivity and selectivity of the cross-catalytic circuit.....	S16
Figure S9. Sensitivity of the non-feedback circuit.....	S17
Figure S10. Schematic illustration of the updated miR-21-targeting cross-catalytic circuit.....	S18
Figure S11. Optimization of the miR-21-recognizing auxiliary hairpin H_p	S19
Figure S12. Selectivity of the updated miR-21-sensing platform.....	S20
Figure S13. Performance of the cross-catalytic amplifier in serum samples.....	S21
Figure S14. Flow cytometry of MCF-7 cells.....	S22
Figure S15. Cross-catalytic intracellular imaging of miR-21 with different expressions.....	S23
References	S24

Supporting Information

Experimental Section

Chemicals and materials

4-(2-Hydroxyethyl) piperazine-1-ethanesulfonic acid (HEPES), HEPES sodium salt, sodium chloride and magnesium chloride were obtained from Sigma-Aldrich (MO, USA). All the chemicals were analytical reagents and used without further purification. DNase/RNase-Free Deionized Water was purchased from TIANGEN Biotech Co., Ltd. (Beijing, China). DEPC-treated ultrapure water ($\geq 18\text{ M}\Omega$, Milli Q, Millipore) was used in the preparation of aqueous solutions. All cell lines were purchased from Shanghai Institutes for Biological Sciences (SIBS). Cell medium was obtained from HyClone (Logan, Utah, USA). Oligonucleotides containing ribonucleobase were purchased from Takara Biotechnology Co., Ltd. (Dalian, China). Other oligonucleotides were synthesized by Sangon Biotech Co., Ltd. (Shanghai, China). All oligonucleotides were purified by high performance liquid chromatography (HPLC) and dissolved in DNase/RNase-Free Deionized Water before use. DNA hairpins were heated to $95\text{ }^{\circ}\text{C}$ for 5 min and then cooled down to room temperature ($25\text{ }^{\circ}\text{C}$) for 2 h before use. The single-stranded **S** and **L** were incubated together for 1 h to generate double-stranded **S-L** before use. The sequences of all oligonucleotides are exhibited in **Tables S3**.

Fluorescence assays

All assays were carried out in reaction buffer (10 mM HEPES, pH 7.2, 100 mM NaCl and 20 mM MgCl_2), and the reaction mixtures were incubated at $30\text{ }^{\circ}\text{C}$ for 5 h. Unless specifically indicated, the concentrations of hairpins and **S** were fixed at 100 nM and the concentration of **L** was 130 nM. All fluorescence measurements were captured using a Cary Eclipse Fluorescence Spectrophotometer (Agilent Technologies, USA). For analyte detection, different concentrations of analytes were added into probe solution. After reaction, the fluorescence emission spectra were recorded between 500 and 650 nm at an excitation wavelength of 488 nm in a 200 μL quartz cuvette. In optimal experiments and kinetic study, analytes of 10 nM were employed. The fluorescence intensities and time dependent fluorescence changes were obtained at a fixed wavelength of 520 nm.

Native polyacrylamide gel electrophoresis

Gel electrophoresis assays were applied to directly characterize the nucleic acid circuits. To improve the quality of images, the concentrations of **T** and **Dz** were set at 100 nM, the concentrations of hairpins and **S** were fixed at 400 nM, and the concentration of **L** was 520 nM. All DNA samples were incubated at $30\text{ }^{\circ}\text{C}$ for 5 h. Then, 10 μL resultant samples were mixed with 2 μL 6 \times loading buffer, which was followed by 12% native polyacrylamide gel electrophoresis. The electrophoresis was executed at 120 V for 90 min in 1 \times TBE buffer (89 mM Tris, 89 mM boric acid, 2.0 mM EDTA, pH 8.3). The gel was then dyed with GelRed and analysed by FluorChem FC3 (ProteinSimple, USA) under 365 nm UV irradiation.

Cell culture and transfection of updated cross-catalytic circuit

MCF-7 cells (human breast cancer cells) and HeLa cells (human cervical carcinoma cells) were cultured in DMEM (Dulbecco's Modified Eagle Medium) containing 10% FBS (fetal bovine serum) and 1% penicillin-streptomycin. MRC-5 cells (human embryonic lung fibroblast) were grown in MEM Alpha Modification supplemented with 10% FBS and 1% penicillin-streptomycin. All cell lines were incubated in a cell culture incubator at $37\text{ }^{\circ}\text{C}$ with humidified atmosphere containing 5% CO_2 and 95% air. Cells were plated on a dish with glass bottom and incubated in 1 mL culture medium at $37\text{ }^{\circ}\text{C}$ for 12 h. The biosensing mixture consists of **H_p**, **H₁**, **H₂**, **S** (0.2 nmol each) and **L** (0.26 nmol) was prepared in 200 μL Opti-MEM, and then mixed with lipofectamine 3000 (5 μL) diluted in 200 μL Opti-MEM for 10 min. Then the plated cells were incubated in the aforesaid mixture supplemented with 20% FBS at $37\text{ }^{\circ}\text{C}$ for 5 h. Subsequently, the cells were washed with PBS buffer (phosphate buffered saline) three times for confocal fluorescence imaging. To adjust the concentration of miR-21 in living cells, MCF-7 cells were respectively transfected with miR-21-mimicking strands or anti-miR-21 strands (final concentration 100 nM) in advance for 2 h.

Confocal fluorescence imaging

The confocal fluorescence images of living cells were acquired using Leica TCS SP8 laser scanning confocal microscope with Leica Application Suite Advanced Fluorescence (LAS-AF) software system. All images were taken under a water dipping objective (63 \times 1.4). The green channel of FAM fluorescence was obtained using an external 488 nm excitation. The confocal fluorescence images were presented after processing by ImageJ software.

Flow cytometry

MCF-7 cells were seeded in a six-well culture plate and cultured in culture medium at $37\text{ }^{\circ}\text{C}$ for 12 h. Then the MCF-7 cells were transfected with the cross-catalytic system (0.2 nmol **H_p**, **H₁**, **H₂**, **S** and 0.26 nmol **L**) or the non-feedback system (0.2 nmol **H_p**, **H₁**, **H₂**, **S_c** and 0.26 nmol **L**). After transfection for 5 h, cells were washed three times with 1 \times PBS and detached from the six-well culture plate by trypsin. After washing the cells with PBS and centrifuging at 1300 rpm for 4 min, flow cytometry was performed using a CytofLEX system (Beckman Coulter, US.) under 488 nm excitation. Fluorescence intensities represented 10^4 analyzed cells.

Simulation method

The simulations of the reaction kinetics were carried out using MATLAB program. Firstly, all reaction formulas were modeled using differential equations. Secondly, the experimental data were used to estimate the unknown parameters in the mathematical model through ode45 function. Finally, based on mathematical model, the reaction process was simulated using updated parameters. More details can be found in supplementary modeling section.

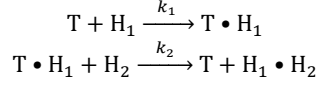
Supporting Information

Modeling Section

Cross-catalytic CHA-DNAzyme circuit modeling

According to **Scheme 1**, the cross-catalytic reaction can be roughly categorized into the CHA reaction initiated by trigger **T**, the DNAzyme-catalyzed digestion of **S-L** substrate, the asymptotic leakage of CHA reaction, the CHA leakage caused by **S-L** disassembly and **S-L** degradation. Here **S** is used to represent **S-L** substrate in equations.

The CHA reaction initiated by trigger **T** can be modeled using the following reactions:



To make the CHA reaction feasible for analytical treatment, the following simplifying assumptions were made:

- **Assumption 1.** The two reactions are irreversible. This approximation is proved through multi-stranded partition function analysis with NUPACK (www.nupack.org).
- **Assumption 2.** The two reaction rate constants are same: $k_1=k_2=k_{app}$. This assumption is rational because both the strand-displacement reactions are mediated by 7-nt toeholds. Under the experimental conditions, the reaction rate of the strand-displacement reaction is mainly dependent on the toehold length.
- **Assumption 3.** The amount of consumed **H₁** monomer is considered the same with that of consumed **H₂** monomer. The assumption is reasonable because two hairpins are cross-opened. In addition, the initial concentrations of **H₁** and **H₂** monomers are the same, $[H]_0 = [H_1]_0 = [H_2]_0$, then we can get

$$\begin{aligned} [H]_t &= [H_1]_t = [H_2]_t \\ [H_1 \cdot H_2]_t &= [H]_0 - [H]_t \end{aligned}$$

- **Assumption 4.** The cleaved **S-L** substrate can immediately and completely release the pre-protected trigger **T** to initiate the CHA reaction. Thus, we can get

$$[T]_t + [T \cdot H_1]_t = [T]_0 + [S]_0 - [S]_t$$

Under the above assumptions, the CHA reaction can be modeled as the follows:

$$-\frac{d[H_1]}{dt} = k_{app} * [T]_t * [H_1]_t \quad (1)$$

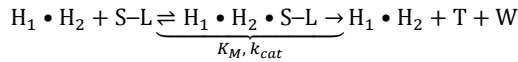
$$-\frac{d[H_2]}{dt} = k_{app} * [T \cdot H_1]_t * [H_2]_t \quad (2)$$

By integrating equations (1) and (2), then we can get

$$-\left(\frac{d[H_1]}{dt} + \frac{d[H_2]}{dt}\right) = -2 \times \frac{d[H]}{dt} = k_{app} * ([T]_t + [T \cdot H_1]_t) * [H]_t = k_{app} * ([T]_0 + [S]_0 - [S]_t) * [H]_t \quad (3)$$

$$-\frac{d[H]}{dt} = 1/2 * k_{app} * ([T]_0 + [S]_0 - [S]_t) * [H]_t \quad (4)$$

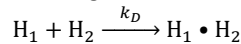
The CHA reaction leads to the assembly of Mg^{2+} -dependent DNAzyme, thus enabling the digestion of **S-L** substrate. Here parameters K_M and k_{cat} were introduced to model the DNAzyme-catalyzed digestion of **S-L** substrate. The digestion reaction can be modeled using the following mechanism:



Thus the digestion reaction can be modeled by equation

$$-\frac{d[S]}{dt} = \frac{k_{cat} * [H_1 \cdot H_2]_t * [S]_t}{K_M + [S]_t} = \frac{k_{cat} * ([H]_0 - [H]_t) * [S]_t}{K_M + [S]_t} \quad (5)$$

The asymptotic leakage of CHA reaction represents the slow, uncatalyzed hybridization of **H₁** and **H₂** monomers due to conformational fluctuations. To take the asymptotic leakage into account, we introduce the parameter k_D to represent the rate constant of the asymptotic leakage. Thus the asymptotic leakage can be modeled through the following reaction:



Therefore, this leakage reaction can be modeled by the equation

$$-\frac{d[H]}{dt} = k_D * [H_1]_t * [H_2]_t = k_D * [H]_t^2 \quad (6)$$

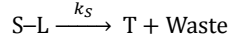
The disassembly of **S-L** substrate may uncover the pre-protected trigger **T**, thus initiating the CHA reaction and leading to signal leakage. To evaluate the signal leakage caused by the disassembly of **S-L** substrate, the parameter k_P is introduced as the rate constant of this leakage reaction. Similar to the CHA reaction initiated by **T**, the leakage caused by **S-L** substrate can be modeled as follows:

$$-\frac{d[H]}{dt} = 1/2 * k_P * ([S]_t + [S \cdot H_1]_t) * [H]_t = 1/2 * k_P * [S]_0 * [H]_t \quad (7)$$

Supporting Information

$$-\frac{d[S]}{dt} = k_P * [S]_t * [H]_t \quad (8)$$

Moreover, the self-degradation of the **S-L** substrate leads to the release of trigger **T**, thus resulting in signal leakage. Therefore, the parameter k_S is introduced to express the reaction rate of the S-L self-degradation. The self-degradation reaction can be modeled using the following reaction



Thus the self-degradation of the **S-L** substrate is modeled as follows:

$$-\frac{d[S]}{dt} = k_S * [S]_t \quad (9)$$

According to the above equations (4) to (9), the cross-catalytic reaction is modeled by state equations:

$$-\frac{d[H]}{dt} = 1/2 * k_{app} * ([T]_0 + [S]_0 - [S]_t) * [H]_t + k_D * [H]_t^2 + 1/2 * k_P * [S]_0 * [H]_t \quad (10)$$

$$-\frac{d[S]}{dt} = \frac{k_{cat} * ([H]_0 - [H]_t) * [S]_t}{K_M + [S]_t} + k_P * [S]_t * [H]_t + k_S * [S]_t \quad (11)$$

The kinetics of the cross-catalytic circuit is followed with the fluorescence reporter **H₂**, thus we can get an output equation

$$\frac{dF}{dt} = -\alpha * \frac{d[H]}{dt} \quad (12)$$

where α represents a coefficient constant between the fluorescence readout and the concentration of hairpin monomer. The coefficient constant (α) was calculated based on the fluorescence experimental data. The correlation between F_t and the concentration of CHA monomer can be described as follows:

$$F_t = -\alpha * [H]_t + k \quad (13)$$

At the beginning of the reaction, $[H]_0 = 100 \text{ nM} = 1 \times 10^{-7} \text{ M}$, thus the equation (13) can be written as follows:

$$F_0 = -10^{-7} * \alpha + k \quad (14)$$

After the reaction reaches the equilibrium state, the hairpin monomer is theoretically completely consumed. Therefore, the equation (13) can be written as follows:

$$F_\infty = k \quad (15)$$

According to the equations (14) and (15), the coefficient constant (α) can be represented as follows:

$$\alpha = (F_\infty - F_0) / 10^{-7} \quad (16)$$

Therefore, the initial fluorescence intensity and the fluorescence intensity at equilibrium can be substituted into the equation (16) to obtain the corresponding coefficient constant (α).

The equations (10) to (12) were implemented in MATLAB program to simulate the cross-catalytic circuit. The experimental kinetic traces shown in **Figure 1B** were used to estimate the unknown parameters in the mathematical model through ode45 function. Based on mathematical model, the reaction process was simulated using updated parameters. The average rate constants of the cross-catalytic circuit were summarized in **Table S1**.

Non-feedback circuit modeling

The components of the non-feedback circuit are the same as that of the cross-catalytic circuit. Therefore, the mathematical model of the cross-catalytic model can be applied to the non-feedback circuit. However, the substrate hybrid in the non-feedback circuit can efficiently block the digestion due to the absence of ribonucleotide site (rA). Thus the rate constants K_M , k_{cat} and k_S are close to zero. To simplify the simulation, we assume that the rate constants K_M , k_{cat} and k_S are equal to zero. Therefore, the non-feedback circuit is modeled by equations

$$-\frac{d[H]}{dt} = 1/2 * k_{app} * [T]_0 * [H]_t + k_D * [H]_t^2 + 1/2 * k_P * [S]_0 * [H]_t \quad (17)$$

$$\frac{dF}{dt} = -\alpha * \frac{d[H]}{dt} \quad (18)$$

The equations (17) to (18) were used to simulate the non-feedback circuit. The corresponding rate constants were summarized in **Table S2**.

Supporting Information

Table S1. Rate constants of the cross-catalytic circuit.

$[T]_0$ (nM)	k_{app} ($M^{-1}\cdot min^{-1}$)	k_D ($M^{-1}\cdot min^{-1}$)	k_P ($M^{-1}\cdot min^{-1}$)	k_{cat} (min^{-1})	K_M (M)	k_S (min^{-1})
0	8.60×10^5	7.65×10^2	20.20	1.01×10^{-2}	3.03×10^{-7}	1.08×10^{-7}
0.5	8.70×10^5	6.35×10^2	24.20	1.11×10^{-2}	2.83×10^{-7}	1.18×10^{-7}
1	8.42×10^5	5.05×10^2	19.20	1.23×10^{-2}	2.78×10^{-7}	1.33×10^{-7}
5	8.41×10^5	6.15×10^2	20.20	1.8×10^{-2}	3.43×10^{-7}	1.05×10^{-7}
10	8.87×10^5	7.25×10^2	33.20	2.92×10^{-2}	3.08×10^{-7}	2.08×10^{-7}
Average	8.60×10^5	6.49×10^2	23.40	1.49×10^{-2}	3.03×10^{-7}	1.34×10^{-7}

Supporting Information

Table S2. Rate constants of the non-feedback circuit.

$[T]_0$ (nM)	k_{app} ($M^{-1}\cdot min^{-1}$)	k_D ($M^{-1}\cdot min^{-1}$)	k_P ($M^{-1}\cdot min^{-1}$)
0	8.49×10^5	7.61×10^2	30.70
1	8.59×10^5	6.21×10^2	20.70
2	8.56×10^5	6.01×10^2	21.20
5	8.55×10^5	5.81×10^2	23.70
10	8.15×10^5	3.81×10^2	23.70
Average	8.47×10^5	5.89×10^2	24.00

Supporting Information

Table S3. Sequences of all oligonucleotides used in this work.

No.	Sequence (5'→3')
H₁	5'-TGA TAA GAT GGG TGT AGG AAG TGC CAC AAG TAC ACT TCC TAC ACC CAT GTA CTG ATA-3'
H_{1A}	5'-TGA TAA GAT GGG TGT AGG AAG TGC CAC AAG TAC ACT TCC TAC ACC CAT GTA CAG TCA-3'
H₂	5'-GGT AAC AGC GAT TAG GAA GT (-FAM) G TAC TTG TGG CAC TTC CTA CAC CCA TTG CCA CAA GTA CA-TAMRA-3'
H_{2A}	5'-GTC ATT CAG CGA TTA GGA AGT GTA CTT GTG GCA CTT CCT ACA CCC ATT GCC ACA AGT ACA-3'
H_P	5'-TCA GAC TGA TGT TGA TGC TTC CTA CAC CCA TCT TAT CAT CAA CAT CAG TCT GAT AAG CTA-3'
S	5'-CTT CCT ACA CCC ATC TTA TCA GTT rA GG TTA CCC ATC GAC CAT CAG TTT CAC AGA C-3'
S_A	5'-FAM-TGA CTG TT rA GGA ATG AC-BHQ-3'
S_C	5'-CTT CCT ACA CCC ATC TTA TCA GTT AGG TTA CCC ATC GAC CAT CAG TTT CAC AGA C-3'
L	5'-GTC TGT GAA ACT GAT GGT CGA TGT TTT TAG TTG GCT GTA GGA AG-3'
L_A	5'-GTC TGT GAA ACT GAT GGT CGA TGT TTT TAG ATG CGT GTA GGA AG-3'
L_B	5'-GTC TGT GAA ACT GAT GGT CGA TGT TTT TAG TTG GCT GTA GGA A-3'
D_z	5'-GGT AAC AGC GAT TAA CGG CGT TAT TTT ACG CCG TTA CAC CCA TGT ACT GAT A-3'
T	5'-CTT CCT ACA CCC ATC TTA TCA-3'
T₁	5'-CTT CCT ACA CCG ATC TTA TCA-3'
T₂	5'-CTT CCT ACA CCG ATC TTT TCA-3'
T₃	5'-CTT CCA ACA CCG ATC TTT TCA-3'
miR-21	5'-UAG CUU AUC AGA CUG AUG UUG A-3'
miR-144	5'-UAC AGU AUA GAU GAU GUA CU-3'
Let-7a	5'-UGA GGU AGU AGG UUG UAU AGU U-3'
miR-429	5'-UAA UAC UGU CUG GUA AAA CCG U-3'
miR-155	5'-UUA AUG CUA AUC GUG AUA GGG GU-3'
miR-21 mimics	5'-TAG CTT ATC AGA CTG ATG TTG A-3'
anti-miR-21	5'-TCA ACA TCA GTC TGA TAA GCT A-3'

Supporting Information

Table S4. Comparison of different enzyme-free strategies for microRNA detection.

System	Sensing duration (h)	Sensitivity (M)	Ref.
Gold nanoparticle-loaded DNAzyme probe for amplified miRNA detection in living cells	8	1.0×10^{-11}	[1]
CHA-DNAzyme-mediated microRNA detection and intracellular imaging	5	1.0×10^{-11}	[2]
Localized catalytic hairpin assembly reaction for microRNA imaging in live cells	1	2.0×10^{-12}	[3]
Autonomous hairpin DNA cascade reaction for mRNA imaging in live cells	2	5.0×10^{-10}	[4]
FRET-based hybridization chain reaction for <i>in situ</i> visualization of mRNA	4	1.8×10^{-11}	[5]
DNAzyme-powered cross-catalytic circuit for amplified intracellular imaging	5	1.56×10^{-11}	This work

Supporting Information

Schematic illustration of the CHA reaction.

As schematically illustrated in **Figure S1**, target **T** (a-b-c) is complementary to the toehold (domain c*) and the stem region (b*-a*) of **H₁**. During the CHA reaction, target **T** can open **H₁** through toehold-mediated branch migration reaction to yield **T-H₁** duplex. Meanwhile, the newly exposed single-stranded domain a-d of the resulting **T-H₁** structure nucleates at the sticky end (domain a*) of **H₂** to operate the branch migration, leading to the formation of an intermediated structure **T-H₁•H₂**. Then, a disassembly process is executed, in which **H₂** displaces **T** from the intermediated complex to generate **H₁•H₂** duplex. Meanwhile, the displaced **T** is free to catalyze the next round of assembly between **H₁** and **H₂**.

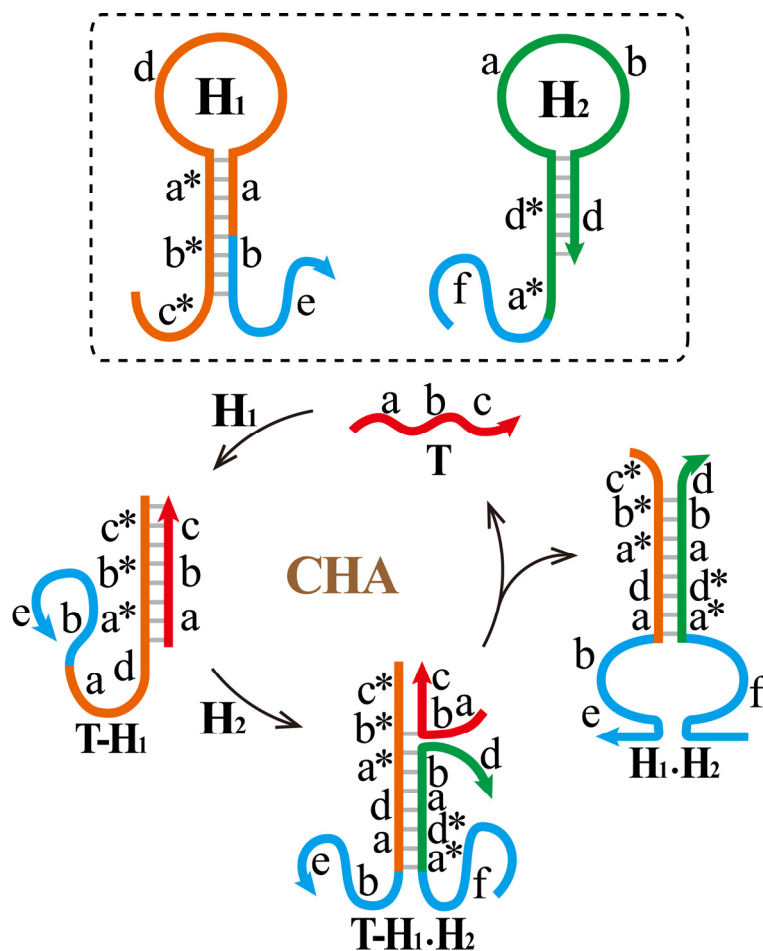


Figure S1. Schematic representation of the CHA circuit.

Supporting Information

Demonstration of the lead-in CHA-DNAzyme concatenation.

Firstly, the lead-in CHA-DNAzyme concatenation is established for investigating the transmission of CHA to DNAzyme in a cascaded manner. As shown in **Figure S2(A)**, the lead-in CHA-DNAzyme concatenation is made up of two catalytic YES gates following the hierarchical principle: CHA gate \rightarrow DNAzyme gate. In CHA gate, the input **T** initiates the CHA reaction for assembling active DNAzyme. Subsequently, the generated DNAzyme feed forward to the next DNAzyme gate for catalytically cleaving the corresponding RNA-modified substrate **S_A**. The reliability of our CHA gate was demonstrated by PAGE (**Figure S2(B)**), thus enabling us to further explore the integrated lead-in CHA-DNAzyme concatenation by fluorescence experiment. As exhibited in **Figure S2(C)**, an obviously increased fluorescence output is revealed when input **T** was added into the proposed concatenation reactants (curve a). In contrast, a slight increment of fluorescence intensity is shown for the lead-in CHA-DNAzyme concatenation without input **T** (curve a'). Clearly, the lead-in CHA-DNAzyme concatenation can specifically respond to the importation of input as designed expectantly.

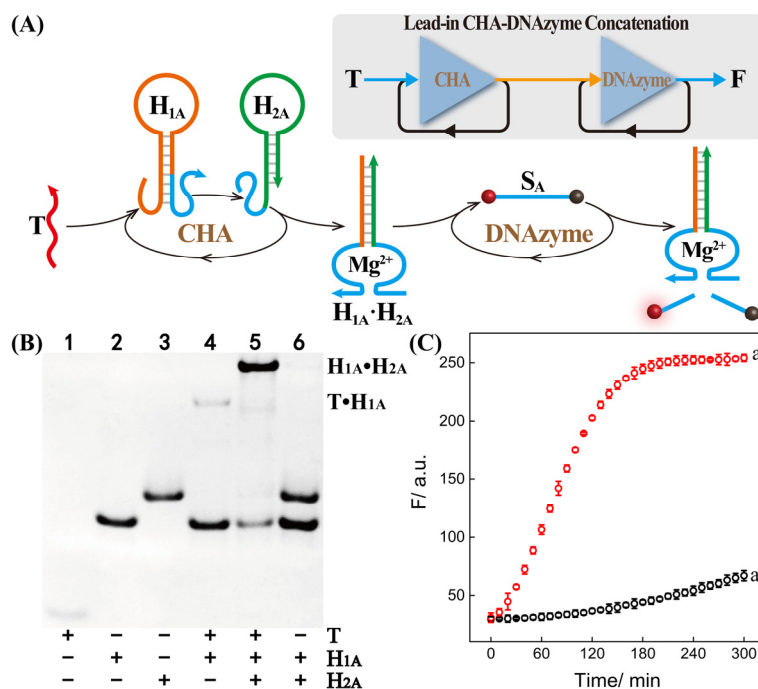


Figure S2. (A) Schematic representation of the lead-in CHA-DNAzyme concatenation. (B) Native gel electrophoresis investigation of CHA reaction. The symbols “+” and “-” respectively represent the presence and absence of relevant components. (C) The fluorescence monitoring of the concatenated lead-in CHA-DNAzyme circuit upon their incubation with 10 nM input (a) and no input (a'). The error bars indicate mean \pm SD (n = 3).

Supporting Information

Demonstration of the reverse DNAzyme-CHA concatenation.

Then, the reverse DNAzyme-CHA concatenation was constructed (**Figure S3**) based on the following hierarchical principle: DNAzyme gate \rightarrow CHA gate. As displayed in **Figure S3(A)**, the first layer logic gate is driven by a single-stranded Mg^{2+} -dependent DNAzyme (**Dz**) to continuously produce a trigger strand **T** that is applied for specifically triggering the subsequent CHA reaction. Noted that the duplex adduct was designed to possess a loop region that contained a DNAzyme cleavage site (TrAG) and two DNAzyme recognition domains. Upon the DNAzyme-mediated generation of input **T**, the CHA reaction is actuated to generate the $H_{1A} \cdot H_2$ duplex where the fluorophore donor and acceptor are separated. Under this circumstance, the fluorescence of FAM is recovered to exhibit a fluorescence “signal-on” mode. The PAGE experiment was firstly carried out to confirm the feasibility of the present reverse DNAzyme-CHA concatenation (**Figure S3(B)**). To further confirm the performance of our reverse concatenation, the fluorescence assay was also implemented (**Figure S3(C)**). The reverse concatenated circuit shows a significantly higher fluorescence signal upon the activation of **Dz** (curve a), and no significant fluorescence change can be observed in the absence of **Dz** input (curve a’), which indicates that **Dz** cleaves the **S-L** adduct to release trigger **T** for activating CHA reaction.

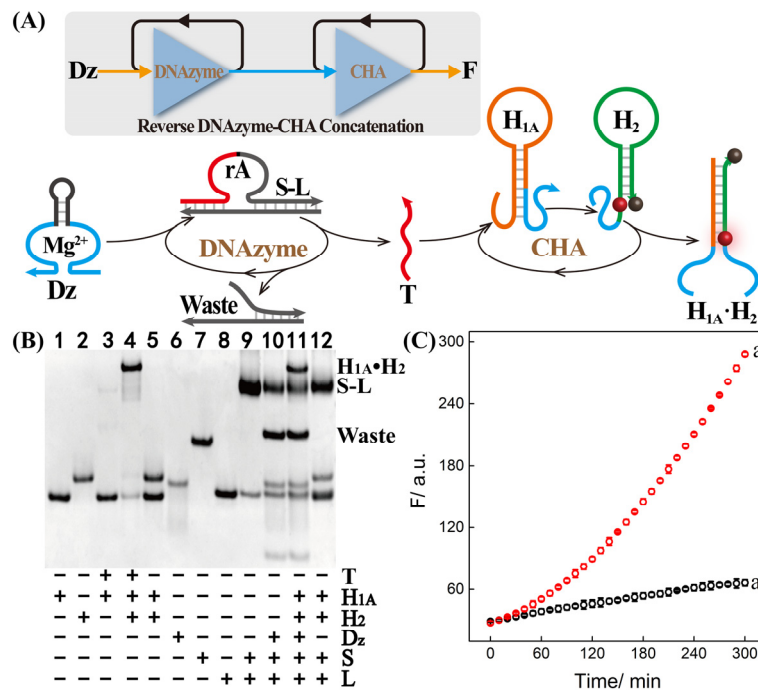


Figure S3. (A) Illustration of the reverse DNAzyme-CHA concatenation. (B) PAGE analysis of the reverse concatenated circuit. The symbols “+” and “-” respectively represent the presence and absence of relevant components. (C) The fluorescence monitoring of the reverse concatenated DNAzyme-CHA circuit upon their incubation with 50 nM input (a) and no input (a’). The error bars indicate mean \pm SD ($n=3$). The concatenation circuit mixture consisting of 100 nM H_{1A} , 100 nM H_2 , 100 nM **S** and 130 nM **L** was reacted at 30 °C in reaction buffer for 5 h to acquire the respective fluorescence spectra.

Supporting Information

Optimization of reaction buffer.

The salt concentration of reaction buffer determines the stability of hairpin and double-stranded structure, thus affecting the signal-to-background ratio of the cross-catalytic circuit. Here the performance of the cross-catalytic circuit was investigated by in 10 mM HEPES containing different salt concentrations (100 mM NaCl, 20 mM MgCl₂ and 1 M NaCl, 50 mM MgCl₂). The corresponding signal-to-background ratios ($\Delta F_S/\Delta F_B$) were shown in **Figure S4**. ΔF_S and ΔF_B represented the fluorescence changes (at $\lambda = 520$ nm) of the system in the presence and absence of 10 nM target **T**, respectively. Obviously, the HEPES buffer containing 100 mM NaCl and 20 mM MgCl₂ showed a higher signal-to-background for cross-catalytic circuit, and was designated as the optimized reaction buffer.

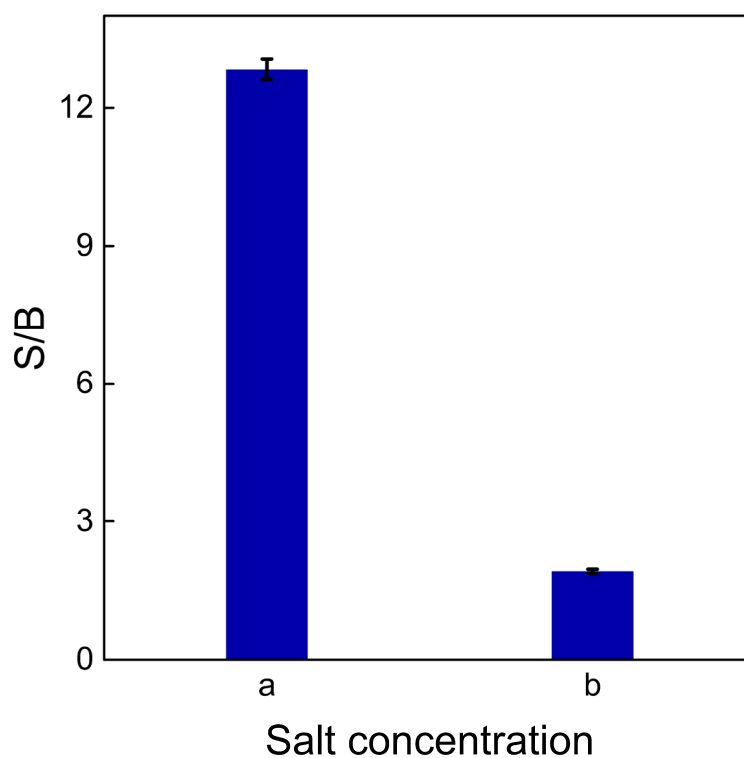


Figure S4. The signal-to-background ratio (S/B) of cross-catalytic circuit in reaction buffer (10 mM HEPES, pH 7.2) containing different salt concentrations: (a) 100 mM NaCl and 20 mM MgCl₂ and (b) 1 M NaCl and 50 mM MgCl₂. The circuit consisting of 100 nM **H**₁, 100 nM **H**₂, 100 nM **S** and 130 nM **L** was incubated at 30 °C for 5 h. The error bars indicate mean \pm SD (n= 3).

Supporting Information

Optimization of reaction temperature.

The reaction temperature affects the hybridization and the stability of DNA duplex, and determines the performance of the cross-catalytic circuit. The circuit was optimized under a series of reaction temperature (25 °C, 30 °C and 37 °C) in the presence and absence of 10 nM T. As shown in **Figure S5**, the circuit executed in 30 °C exhibits the highest signal-to-background ratio, was chosen as the optimized reaction temperature.

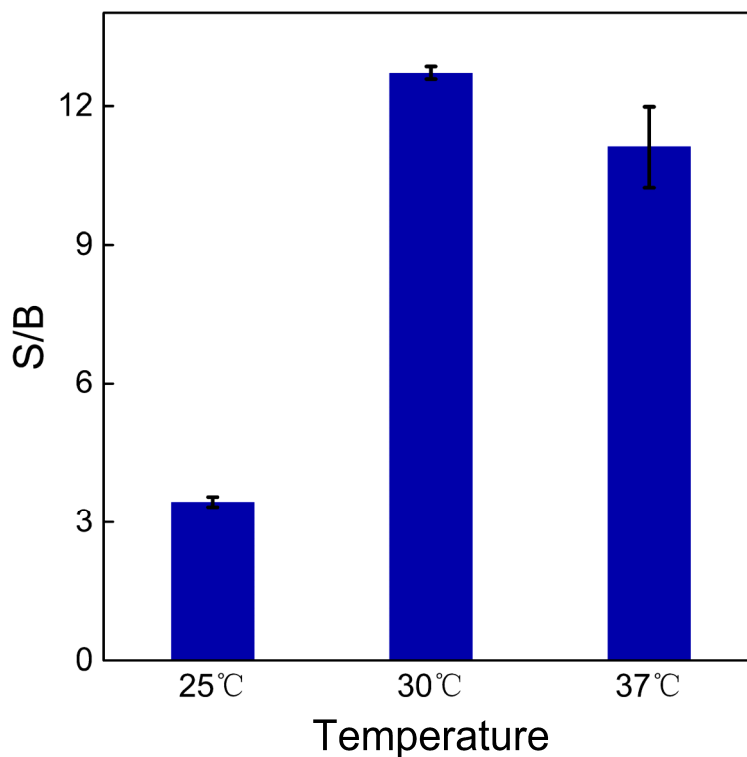


Figure S5. The signal-to-background ratio (S/B) of cross-catalytic circuit executed in different temperature: 25 °C, 30 °C and 37 °C. The circuit consisting of 100 nM H₁, 100 nM H₂, 100 nM S and 130 nM L was carried out in reaction buffer (10 mM HEPES, pH 7.2, 100 mM NaCl, 20 mM MgCl₂) for 5 h. The error bars indicate mean ± SD (n= 3).

Supporting Information

Optimization of substrate blocker L.

Before the DNAzyme-catalyzed digestion of S-L duplex, strand L was used to block the S (hybridize with T' domain) to prevent a possible signal leakage. However, L should be able to release T' after the digestion of S-L duplex. Thus the strand L could affect the performance of cross-catalytic circuit, and needs optimized. Here, three different blocker strands (L_A , L and L_B) were rationally designed and investigated. Here L_A , L and L_B contained one-, two- and three-mismatched bases in the complementary region of T', respectively. The circuits with different blocker strands were used to obtain the corresponding signal-to-background ratio. As shown in **Figure S6**, the circuit exhibited the highest signal-to-background ratio for L, which was selected to constitute a satisfactory cross-catalytic circuit.

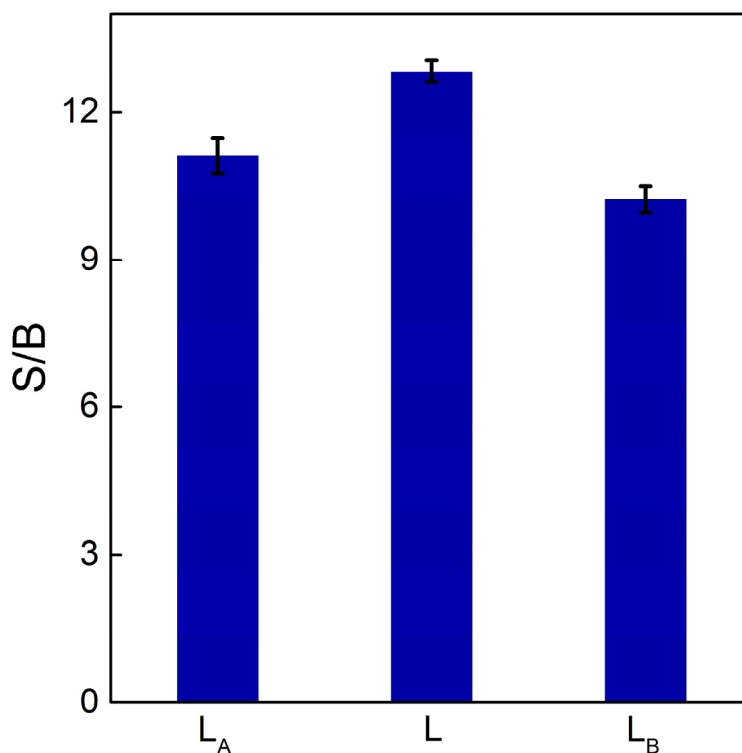


Figure S6. The signal-to-background ratio (S/B) of cross-catalytic circuit consisting of different blocker strands. The circuit (100 nM H_1 , 100 nM H_2 , 100 nM S and 130 nM blocker strand) was carried out in reaction buffer (10 mM HEPES, pH 7.2, 100 mM NaCl, 20 mM $MgCl_2$) at 30 °C for 5 h. The error bars indicate mean \pm SD (n= 3).

Supporting Information

Optimization of the substrate to blocker (S/L) ratio.

In the cross-catalytic circuit, strand **L** is used to inhibit the signal leakage by blocking initiator strand embedded in strand **S**. However, superfluous **L** can hybridize with the dissociative initiator **T** to damp the legitimate CHA reaction. Therefore, the concentration ratio of **S** to **L** was also optimized (**Figure S7**). The system with **S** to **L** of 1:1.3 exhibited the highest signal-to-background ratio, and was adapted to acquire a better performance of the circuit.

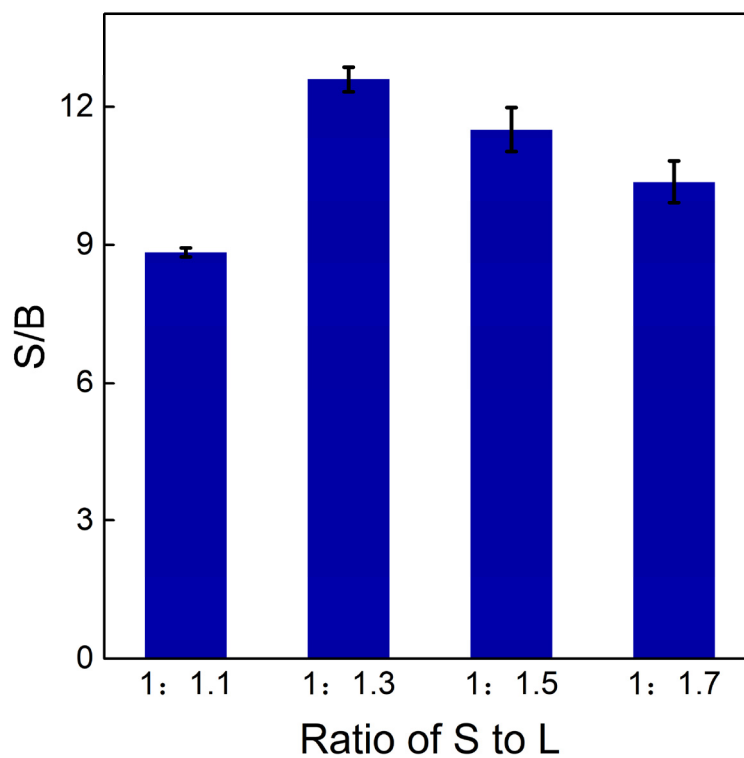


Figure S7. The signal-to-background ratio (S/B) of cross-catalytic circuit with different ratios of **S** to **L**. The circuit consisting of **H₁**, **H₂**, **S** (100 nM each) and **L** was tested in the presence and absence of 10 nM **T** to obtain signal-to-background ratio. The error bars indicate mean \pm SD (n= 3).

Supporting Information

Sensitivity and selectivity of the cross-catalytic circuit.

In the cross-catalytic CHA-DNAzyme circuit, both of the CHA trigger and DNAzyme biocatalyst can not only be regenerated for multiple cycles of biocatalytic reactions, but can also be substantially produced from DNAzyme and CHA reactions, respectively. Therefore, the autocatalytic CHA-DNAzyme circuit is encoded with an accelerated reaction format and a substantially signal amplification feature, thus holding great promise for biosensing applications. The cross-catalytic system reveals a LOD down to **12.8 pM** within the detectable linear range from **10 pM to 1 nM** (Figure S8(A)). The selectivity of the presented cross-catalytic system was elucidated by analyzing target **T** and its one-, two-, and three-nucleotide-mutant analytes (**T₁**, **T₂** and **T₃**, respectively). As shown in Figure S8(B), target **T** contributes an appreciable fluorescence readout, while other mutant analytes generate almost identical fluorescence to blank control. With the favourable sensitivity and selectivity, the proposed cross-catalytic amplification system can serve as a robust and accurate sensing platform for more extensive bioanalytical research fields.

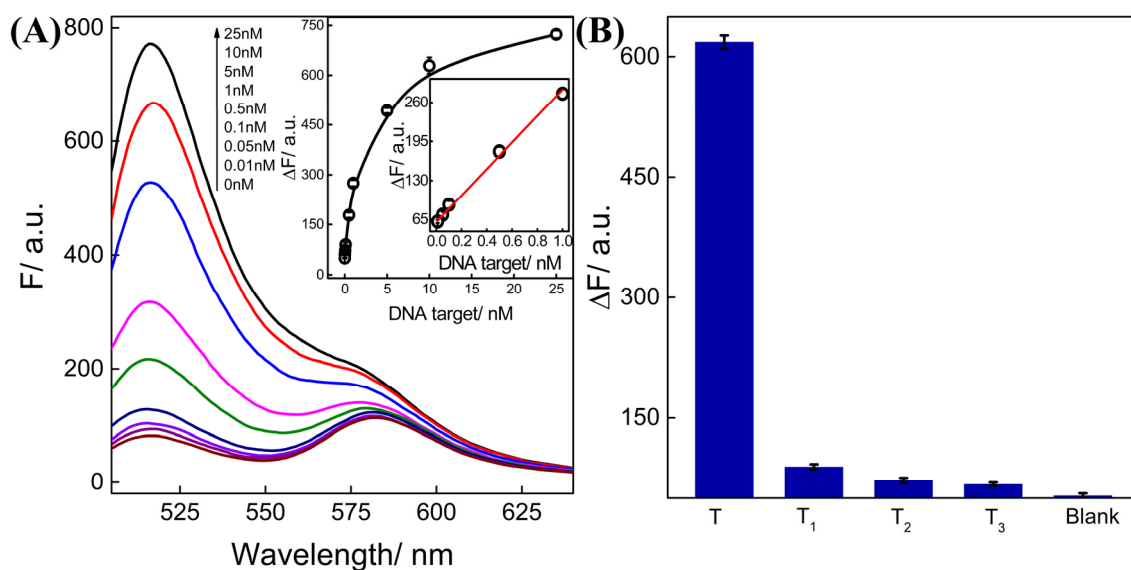


Figure S8. (A) Fluorescence spectra of the cross-catalytic circuit triggered by various concentrations of DNA input. Inset: the corresponding calibration curves. (B) Absolute fluorescence intensities increase (ΔF) of the cross-catalytic circuit upon analyzing 10 nM of different analytes: complementary **T**, one-base mutant **T₁**, two-base mutant **T₂** and three-base mutant **T₃**. The error bars indicate mean \pm SD ($n=3$).

Supporting Information

Sensitivity of the non-feedback circuit.

The non-cross-catalytic system was applied for analyzing different concentrations of target **T**, by recording the fluorescence spectra after a fixed time interval of 5 h (**Figure S9**). An increase of fluorescence intensities was observed as the concentration of target increased, originating from the CHA reaction (**Figure S9(A)**). From the derived calibration curve (**Figure S9(B)**), the detection limit was calculated to be 56.6 pM for the non-cross-catalytic strategy.

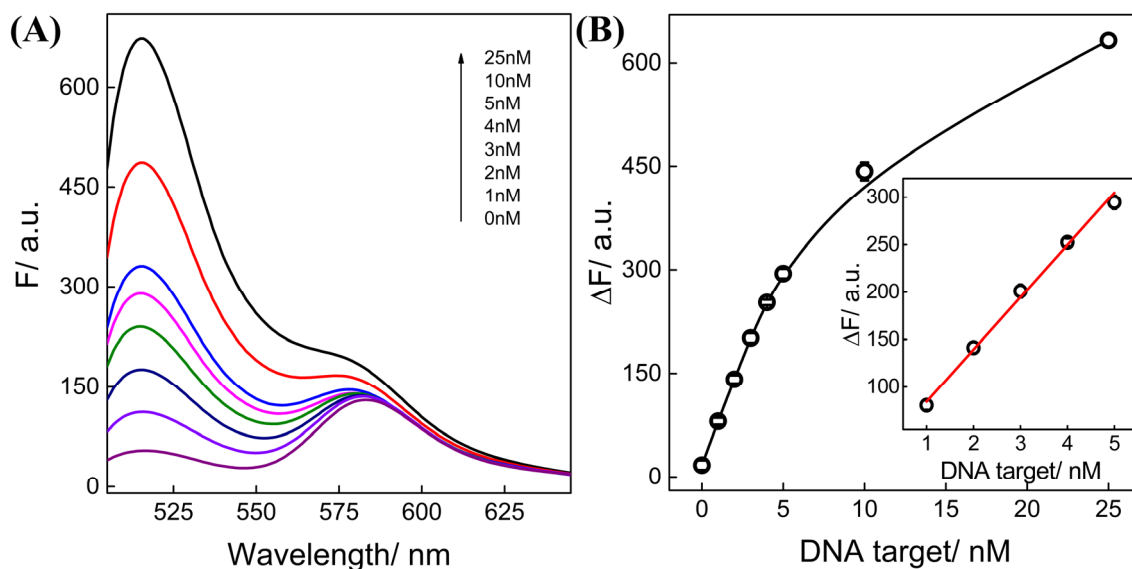


Figure S9. (A) Fluorescence spectra of the non-feedback circuit triggered by various concentrations of DNA input. (B) Corresponding calibration curves as plotting the relationships between the fluorescence intensities and target concentrations. The error bars indicate mean \pm SD ($n=3$). The non-cross-catalytic system (100 nM **H₁**, 100 nM **H₂**, 100 nM **S_C** and 130 nM **L**) was carried out in reaction buffer (10 mM HEPES, pH 7.2, 100 mM NaCl, 20 mM MgCl₂).

Supporting Information

Schematic illustration of updated miR-21-targeting cross-catalytic circuit.

As illustrated in **Figure S10**, the auxiliary hairpin H_P can recognize and hybridize with miR-21 analyte, and subsequently undergoes toehold-mediated strand displacement to release the trigger T . Next, the initiator T feed forward to the cross-catalytic circuit, giving rise to a significantly amplified fluorescence readout signal.

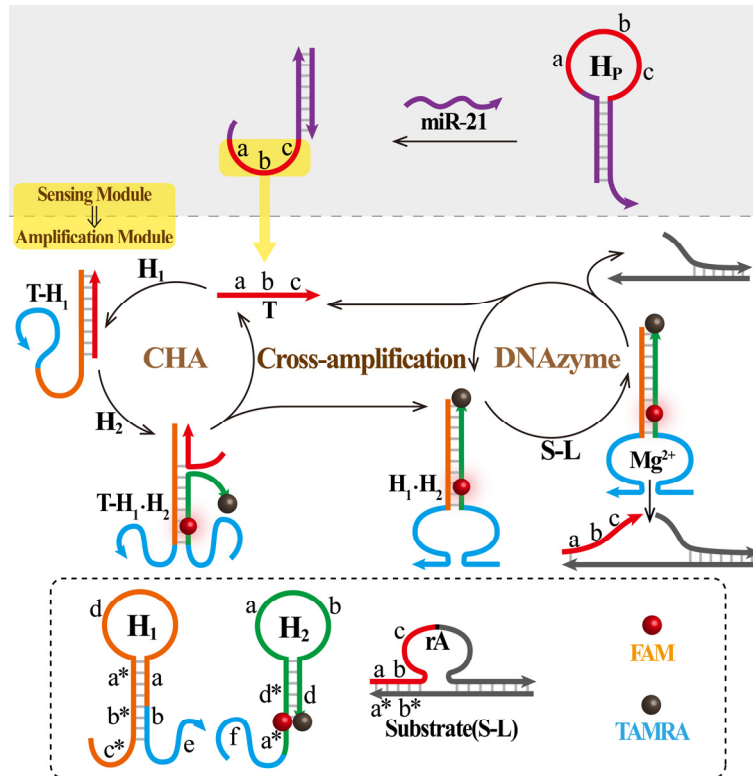


Figure S10. Schematic of the updated miR-21-targeting cross-catalytic circuit.

Supporting Information

Optimization of the miR-21-recognizing auxiliary hairpin H_p .

The updated miR-21-targeting sensing platform is constituted by the cross-catalytic circuit and a “helper” hairpin H_p . The concentration of H_p could affect the performance of the updated system, and was optimized to obtain better performance (Figure S11). Ultimately, the updated system with 100 nM H_p showed the highest signal-to-background ratio and thus chosen as the optimized condition.

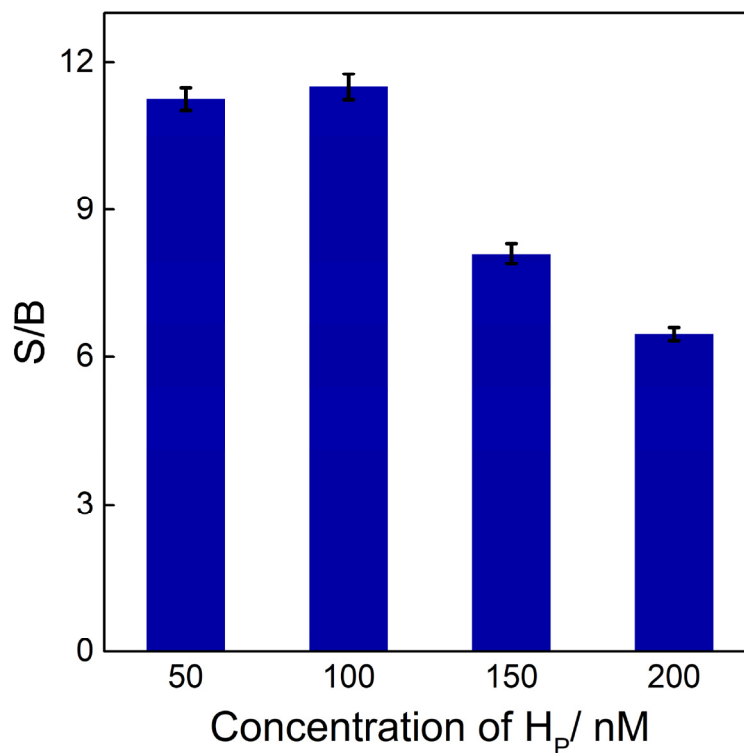


Figure S11. The signal-to-background ratio (S/B) of the updated system when different concentrations of H_p were introduced. The system consisting of H_p , 100 nM H_1 , 100 nM H_2 , 100 nM S and 130 nM L was carried out in reaction buffer (10 mM HEPES, pH 7.2, 100 mM NaCl, 20 mM $MgCl_2$) at 30 °C for 5 h. The error bars indicate mean \pm SD ($n=3$).

Supporting Information

Selectivity of the updated miR-21-sensign platform.

The selectivity of the updated miR-21-sensign platform was assessed by choosing a series of microRNAs as interfere nucleic acids: miR-144, let-7a, miR-429 and miR-155. As shown in **Figure S12**, the miR-21 triggers a substantial higher fluorescence readout while other interfere miRNAs lead to much lower and almost identical fluorescence with blank control, demonstrating the high selectivity of the present autonomously cross-catalytic amplification system.

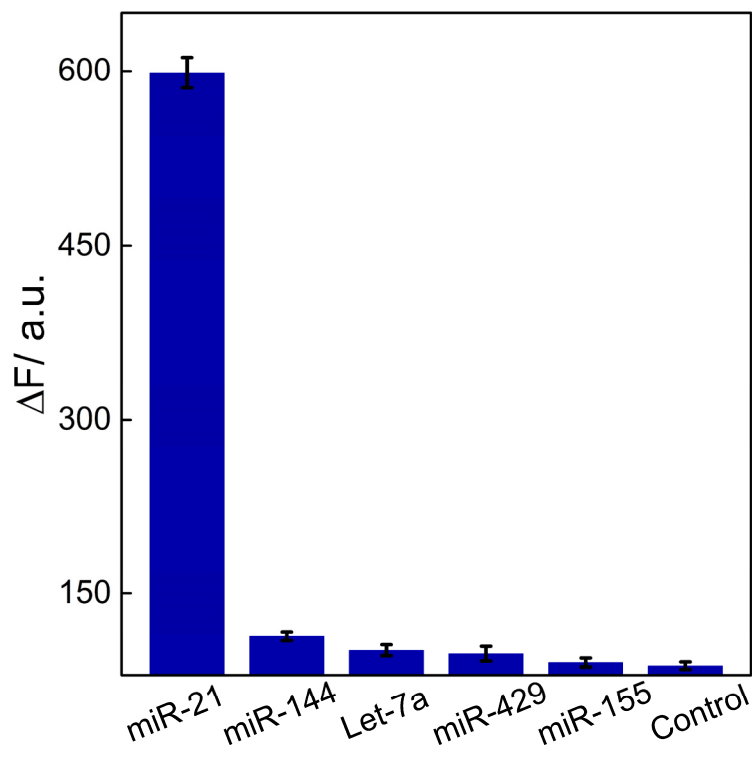


Figure S12. Absolute fluorescence intensity increase (ΔF) of the cross-catalytic cascade system upon analyzing miR-21 and the different interfering analytes. The error bars indicate mean \pm SD ($n=3$).

Supporting Information

Performance of the cross-catalytic amplifier in serum samples.

The stability of the updated biosensing system is crucial for monitoring intracellular miRNA in complex biological environment. Diluted FBS was thus used as reaction buffer to investigate the stability of this updated system. The time-dependent fluorescence changes of the updated system in 0%, 5% and 10% FBS buffer for miR-21 detection were recorded. As shown in **Figure S13**, the performance of the updated cross-catalytic system in dilute FBS was almost identical to that in buffer, indicating that the system possessed moderate resistance to nuclease and kept stable in biological environment, implying their potential in monitoring biomarker (miR-21) in living cells.

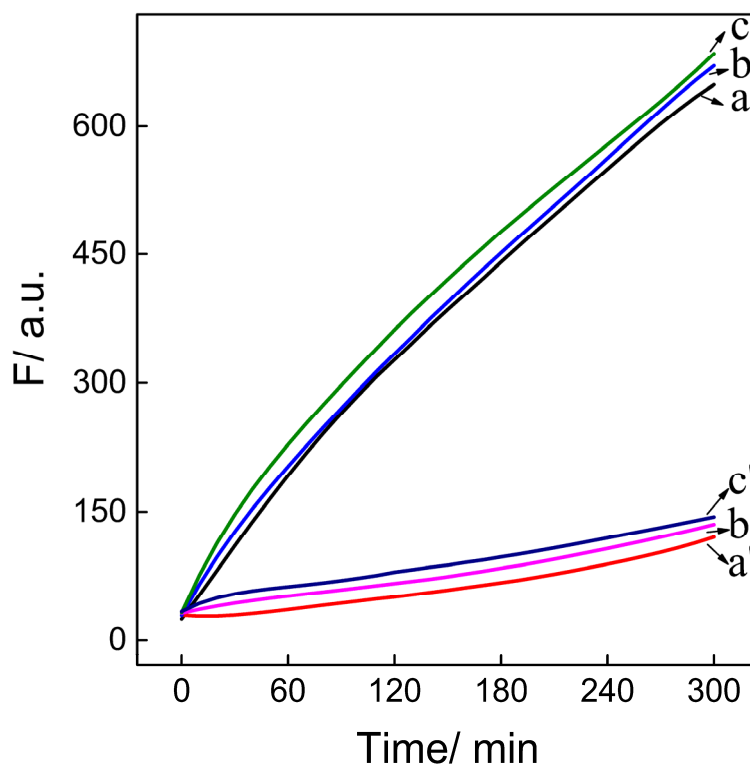


Figure S13. Time-dependent fluorescence changes of the updated biosensing system upon analyzing miR-21 in diluted FBS buffer: (a) 10 nM and (a') 0 nM miR-21 in 0% FBS buffer, (b) 10 nM and (b') 0 nM miR-21 in 5% FBS buffer, and (c) 10 nM and (c') 0 nM miR-21 in 10% FBS buffer. The system consisting of **H_p**, **H₁**, **H₂**, **S** (100 nM each), and **L** (130 nM) was tested at 30 °C for 5 h.

Supporting Information

Flow cytometry of MCF-7 cells treated with the cross-catalytic system and the non-feedback system.

To quantitative the fluorescence of the cross-catalytic and non-feedback circuit in living cells, flow cytometry analysis was further carried out (**Figure S14**). Compared with MCF-7 cells transfected with the non-feedback circuit, the cross-catalytic circuit-transfected MCF-7 cells showed a significantly enhanced fluorescence signal, which was well consistent with the confocal microscopy results. This efficiently demonstrates the high signal amplification ability of the cross-catalytic strategy.

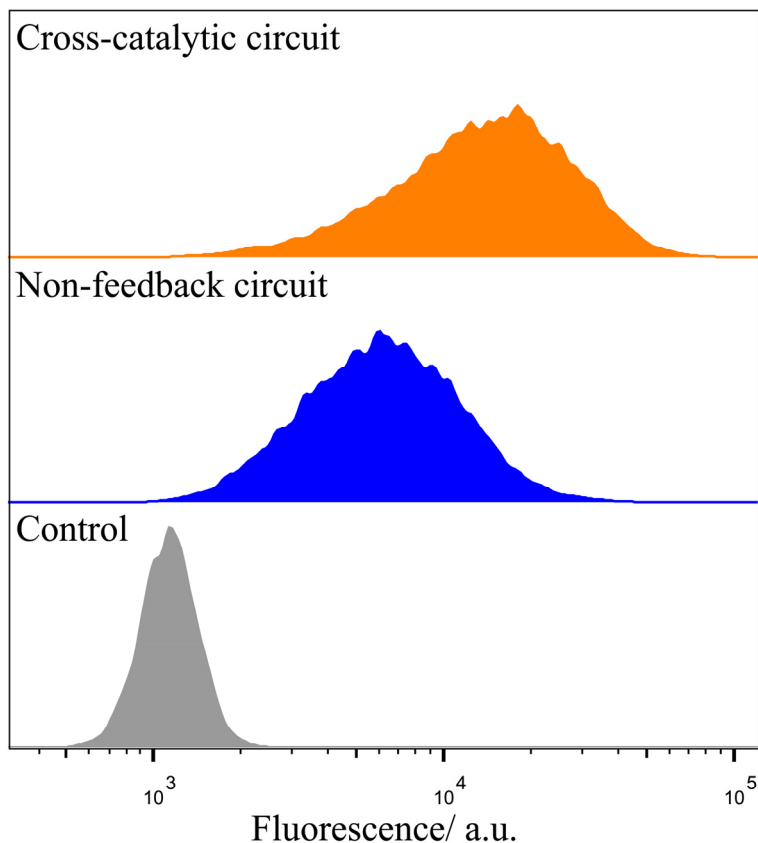


Figure S14. Flow cytometry results of MCF-7 cells treated with the cross-catalytic system and the non-feedback system for 5 h at 37°C. The cross-catalytic system consists of H_p , H_1 , H_2 , S (0.2 nmol each) and L (0.26 nmol). The non-feedback system consists of H_p , H_1 , H_2 , S_c (0.2 nmol each) and L (0.26 nmol).

Supporting Information

Cross-catalytic intracellular imaging of miR-21 with different expressions.

The updated cross-catalytic system was further utilized to identify miR-21 with different levels in MCF-7 cells (**Figure S15**). Here, the intracellular miR-21 was regulated by pre-transfecting with miR-21-mimicking strands and anti-miR-21 strands. Meanwhile, the untreated MCF-7 cells were set as control group. MiR-21-mimicking strand was used to up-regulate the intracellular miR-21 level. As expected, the miR-21-mimics-treated MCF-7 cells showed a higher fluorescence intensity compared with control group. In contrast, anti-miR-21 strand acted as inhibitor that can down-regulate the intracellular miR-21 level. Not surprisingly, the anti-miR-21 strand-pretreated MCF-7 cells showed a lower fluorescence intensity in comparison with untreated MCF-7 cells. The results demonstrated that the updated cross-catalytic system were ultrasensitive to the variations of cell-expressed miRNA in living cells.

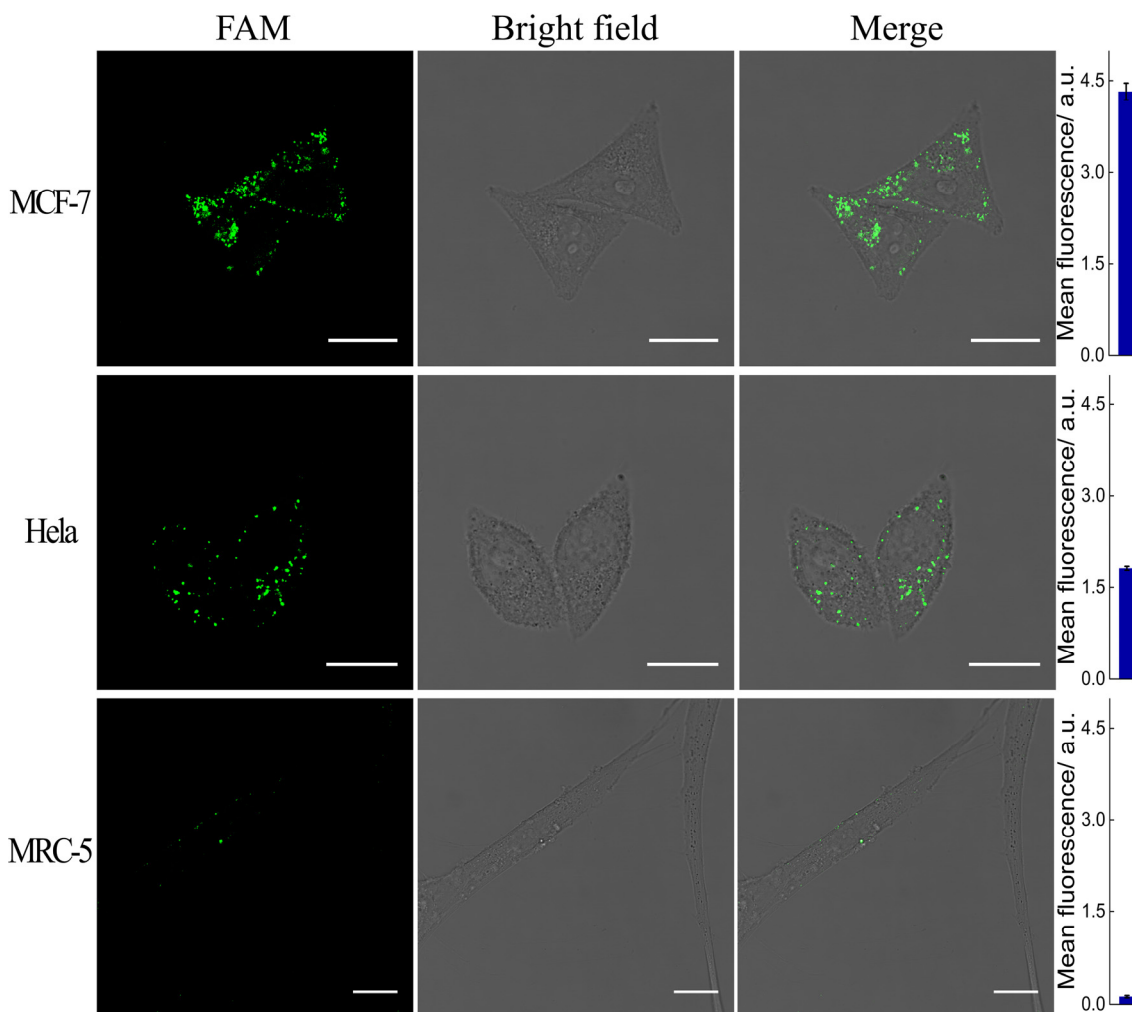


Figure S15. Confocal fluorescence images of MCF-7 cells transfected with miR-21-mimicking strands and anti-miR-21 strands, and untreated MCF-7 cells. The error bars represent the standard deviation of three independent measurements. Cells were pre-treated with miR-21-mimicking strands or anti-miR-21 strands at 37 °C for 2 h, and then were dealt with miR-21-targeting cross-catalytic system at 37 °C for 5 h. All scale bars correspond to 20 μ m.

Supporting Information

References

- 1 Y. Wu, J. Huang, X. Yang, Y. Yang, K. Quan, N. Xie, J. Li, C. Ma and K. Wang, *Anal. Chem.*, 2017, **89**, 8377-8383.
- 2 L. Yang, Q. Wu, Y. Chen, X. Liu, F. Wang and X. Zhou, *ACS Sens.*, 2019, **4**, 110-117.
- 3 Q. Wei, J. Huang, J. Li, J. Wang, X. Yang, J. Liu and K. Wang, *Chem. Sci.*, 2018, **9**, 7802-7808.
- 4 C. Wu, S. Cansiz, L. Zhang, I. T. Teng, L. Qiu, J. Li, Y. Liu, C. Zhou, R. Hu, T. Zhang, C. Cui, L. Cui and W. Tan, *J. Am. Chem. Soc.*, 2015, **137**, 4900-4903.
- 5 J. Huang, H. Wang, X. Yang, K. Quan, Y. Yang, L. Ying, N. Xie, M. Ou and K. Wang, *Chem. Sci.*, 2016, **7**, 3829-3835.